AIAA SciTech Forum
January 3-7, 2022, San Diego, CA & Virtual
AIAA SCITECH 2022 Forum

10.2514/6.2022-1483

Numerical Investigation of the Geometrical Design of a 1 kN Paraffin-Fueled Hybrid Rocket Motor

B. Dequick*, **M. Lefebvre**†
Royal Military Academy, Avenue de la Renaissance 30, Brussels, 1000, Belgium

P. Hendrick‡
Université Libre de Bruxelles, Avenue F.D. Roosevelt 50, Brussels, 1050, Belgium

Since 2010, experimental work has been done with a lab-scale 1 kN paraffin-fueled Hybrid Rocket Motor at Université Libre de Bruxelles (ULB-HRM). The motor uses liquid N_2O as oxidizer and solid paraffin as fuel. To expand the research, a single-phase numerical model of the motor has been developed recently, in 2020. Meanwhile, this model has been improved by including liquid oxidizer spray droplets and entrained fuel droplets in the flow, the latter which is a typical phenomenon in HRMs that use a liquefying fuel such as paraffin. In this paper, a short summary of the most recent two-phase CFD model is provided, followed by a first parametric study of the geometry of the ULB-HRM. It is demonstrated how the lengths of the pre- and post-combustion chamber have an impact on the flowfield, the chamber pressure, and the thrust. It is shown that the extension of both the pre- and post-combustion chamber leads to an increased chamber pressure and thrust. However, for the pre-combustion chamber, these performance parameters stagnate when the extension is more than 50%. The conical nozzle which is installed on the ULB-HRM is under investigation as well. The impact on the thrust of the nozzle half angle and nozzle expansion area ratio is demonstrated. It is shown numerically that the design of the existing nozzle is adequate, within the limiting fact that its shape is conical. Future work includes the numerical design of a minimum length bell-shaped nozzle.

I. Introduction

This work builds upon the ongoing CFD (Computational Fluid Dynamics) work related to the 1 kN lab-scale paraffin-fueled HRM (Hybrid Rocket Motor) at ULB (Université Libre de Bruxelles). This motor, referred to as the ULB-HRM in the remainder of the text, uses liquid N_2O (nitrous oxide) as oxidizer. The fuel is a single-port paraffin fuel grain. Experimental work has been conducted since 2010 [1–4], but the development of a CFD model of the ULB-HRM only started in 2019. A first single-phase model was presented in 2020 [5]. Then, in 2021, this model was improved to a two-phase model by including liquid oxidizer spray and entrained fuel droplets [6]. Compared to the single-phase model, the two-phase model included many additional parameters, mainly related to the droplets diameters and the liquid mass fractions (that is, for example, the fraction of the total oxidizer mass flow rate that enters the domain as liquid droplets). Given the many additional parameters, it was opportune to perform a sensitivity analysis to determine the latest model's robustness. An extensive report on this is presented in [7]. The overall conclusion was that the model performs well, with predictions of the average P_{ch} (chamber pressure) and F (thrust) which deviated, on average, only by +1% and +5% (respectively) from the experimental measurements. Furthermore it was concluded that the model is quite insensitive and it does not suffer from an excessive or abnormal sensitivity to any of the major input parameters. The latest two-phase CFD model is therefore considered to be sufficiently reliable within the boundaries of its purpose, which is to study the impact of certain aspects of the geometrical design of the motor. In the current paper, the model is therefore applied to perform qualitative and quantitative predictions of the motor's performance with varying geometrical parameters. As the two-phase CFD model is summarized only briefly in this paper, the reader is referred to [6, 7] for detailed steps and equations regarding its development, as well as for comprehensive introductions regarding HRMs, CFD, history, and state of the art.

*PhD Candidate
†Professor
‡Professor

II. Summary of the numerical baseline model

The summary in this section is supported by Fig. 1, which provides an overview of all main features of the computational domain and boundary conditions of the numerical model. In this figure, the main flow direction is from left to right. In order to properly relate the geometry of the computational domain to the actual motor, the reader is referred to the 3D-cut of the ULB-HRM design, which is provided in [4, 7]. A picture of the ULB-HRM during operation is presented in [4].

The computational domain is a 2D-axisymmetric domain which is meshed to form a structured-like grid of 120602 cells. It represents the internal geometry of the ULB-HRM as well as an exhaust plume area. In a 2D representation, the mesh almost exclusively consists of quadrilateral cells, with only a few triangular cells near the rounded part of the wall of the pre-combustion chamber.

The flowfield is computed by means of the steady-state RANS (Reynolds-Averaged Navier Stokes) equations together with the standard k-ϵ turbulence model [8]. The liquid droplets are modeled using a discrete phase model in a Lagrangian framework. The discrete liquid phase interacts with the continuous gaseous phase (Eulerian framework) by an exchange of mass, momentum and energy. This exchange appears as source terms in the conservation equations, accounting for the evaporation of droplets, drag forces, and heat exchanges. The discrete droplets do however not interact with each other. Furthermore, they reflect on walls.

The combustion is modeled through the EDM (Eddy Dissipation Model) [9], which uses a global 1-step chemical equilibrium reaction which was determined with ICT-code (thermodynamic code from Fraunhofer Institute for Chemical Technology) [10] and NASA's CEA (Chemical Equilibrium and Applications by the National Aeronautics and Space Administration) [11], which both yield the same result, as it would be expected.

The boundary conditions include an axial gaseous N_2O mass flow inlet as indicated on the left in Fig. 1, as well as an injection of discrete liquid N_2O droplets originating from that same boundary, in order to simulate the injected spray by means of a showerhead injector. The baseline values for the vapor quality (fraction of oxidizer that enters the domain in gaseous form) and the droplets diameter were determined carefully as presented in [7]. Their values are 20% and 100 µm, respectively. Similar boundary conditions are applied for the fuel inlet. 50% of the total inlet fuel mass flow rate consists of liquid paraffin droplets which are injected normal to the grain surface, the latter which is modeled as a wall. The gaseous part of the fuel therefore enters the domain as mass sources in the cells adjacent to the grain surface, rather than as a mass flow inlet. The injected gaseous fuel consists of C_2H_4, which is the main product of pyrolysis of paraffin. Note that the CFD model uses experimental space-time averaged fuel and oxidizer mass flow rates as inputs. In the exhaust plume ambient area, indicated on Fig. 1, an air pressure inlet is set along the lateral boundary, because the exhaust plume draws in air from the sides. The downstream end of the domain is a simple 1 Atm pressure outlet. With this setup, no reversed flows are observed near the edges of the ambient area. The entire engine casing is modeled as adiabatic walls.

The model is developed in ANSYS Fluent and typical computational times for the simulations in the current paper are about 5 hours using an Intel Core i9 2.9 GHz CPU and 64 GB RAM workstation, and about 4 hours on an 80-core 384 GB cluster. Both coupled and SIMPLEC (Semi-Implicit Method for Pressure Linked Equations-Consistent) algorithms are used to obtain converged solutions.

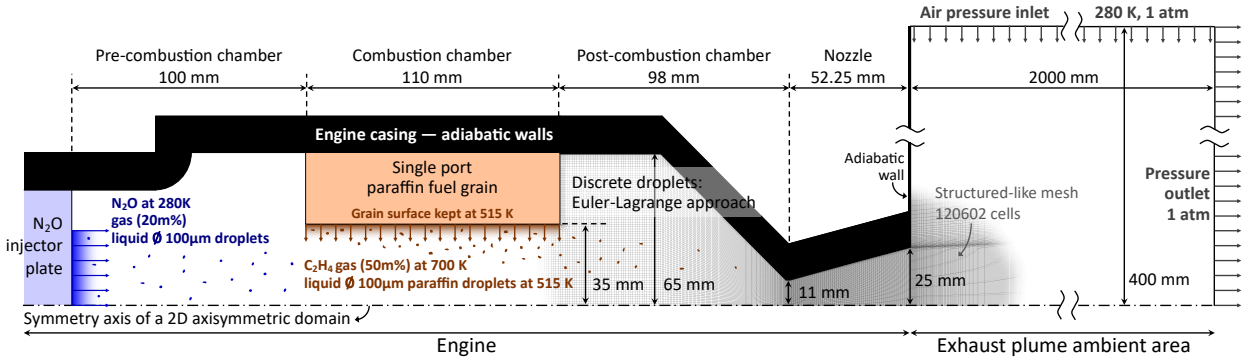

Fig. 1 Overview of the computational domain (white area) and boundary conditions.

III. Investigation of the geometrical design of the ULB-HRM

In this section, the influence of certain geometrical aspects of the ULB-HRM is predicted. Figure 2 summarizes the adopted nomenclature of the dimensions that are under investigation. Only one dimension is changed at a time. Simulations are done for 5 pre-combustion chamber lengths (L_1), 6 post-combustion chamber lengths (L_2), and a series of conical nozzles (parameters L_3, L_4, and α). Note that the indicated nozzle dimensions are obviously not all independent.

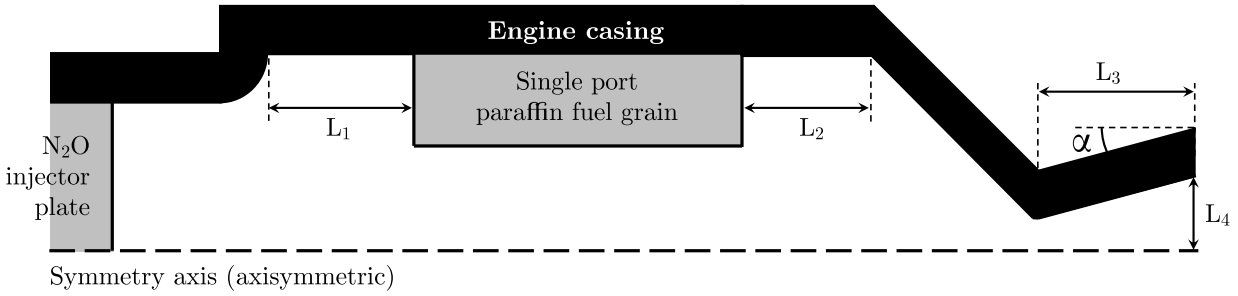

Fig. 2 Overview of the investigated geometrical parameters. Note that the nozzle dimensions are not all independent.

All other parameters (mass flow rates, liquid fractions,...) are those based on the simulation of experiment "SH4-04". Details on the experimental results and the according settings and results of its baseline simulation are presented in [7]. Some key values are given next. The total oxidizer mass flow rate $\dot{m}_{ox}$ is 550 g/s, with a vapor quality x of 20%. The total fuel mass flow rate $\dot{m}_{fuel}$ is 157 g/s, from which 50% is in the form of entrained droplets. The experimental chamber pressure $P_{ch,exp}$ is 24.10 bar and the baseline numerical value $P_{ch,num}$, obtained with the according simulation, is 24.24 bar. For the thrust, F_{exp} = 1172 N and the according F_{num} = 1265 N. These values are regularly indicated on the graphs that follow.

A. Pre-combustion chamber

In this section, the length of the pre-combustion chamber is investigated. Therefore, the baseline value of L_1 is first decreased by 50% and then increased by 50%. To provide additional insight, higher values for L_1 have been selected as well. Table 1 provides an overview of the selected pre-combustion chamber lengths.

Table 1 Selected values for L_1 for the study of its influence on the operating conditions.

L_1 [mm]	Remark
24.33	baseline value −50%
48.65	baseline value
72.98	baseline value +50%
130.0	
200.0	

The resulting static temperature fields for the first 3 values of L_1 are shown in Fig. 3. An increase of L_1 results in a decrease of the temperature in the pre-combustion chamber. This is because the recirculation zone in the pre-combustion chamber reaches less far into the fuel grain port, reducing the amount of fuel that flows upstream into the oxidizer-rich pre-combustion chamber.

Next, the influence of L_1 on the motor's operating conditions is shown in Fig. 4. An important observation is that P_{ch} and F seem to stagnate around 25 bar and 1.28 kN when L_1 becomes larger than 73 mm. It is therefore predicted that there is no advantage in extending the pre-combustion chamber of the ULB-HRM beyond a certain point, which might already be reached at +50%. Before this point, however, it is observed that P_{ch} and F vary almost linearly with L_1.

When taking the three leftmost data points, which correspond to the baseline value of L_1 and its −50% and +50% offsets, the slopes obtained through linear regression are

$$\frac{dP_{\text{ch,num}}}{dL_1} = 0.34 \text{ bar/cm} = (1.4\% \cdot P_{\text{ch,num (baseline)}}) \text{ bar/cm} \quad \text{for } L_1 \in [2.43, 7.30] \text{ cm} \tag{1}$$

$$\frac{dF_{\text{num}}}{dL_1} = 8 \text{ N/cm} = (0.6\% \cdot F_{\text{num (baseline)}}) \text{ N/cm} \quad \text{for } L_1 \in [2.43, 7.30] \text{ cm} \tag{2}$$

When looking at Eq. 1, the pressure change of 0.34 bar (per cm change of L_1) represents 1.4% of the baseline value of $P_{\text{ch,num}}$ which is 24.24 bar. For F, this is only 0.6%. From this it is concluded that the relative influence of L_1 on $P_{\text{ch,num}}$ is higher than on F_{num}. The model predicts that changing the length of the pre-combustion chamber of the ULB-HRM may have little effect on the thrust.

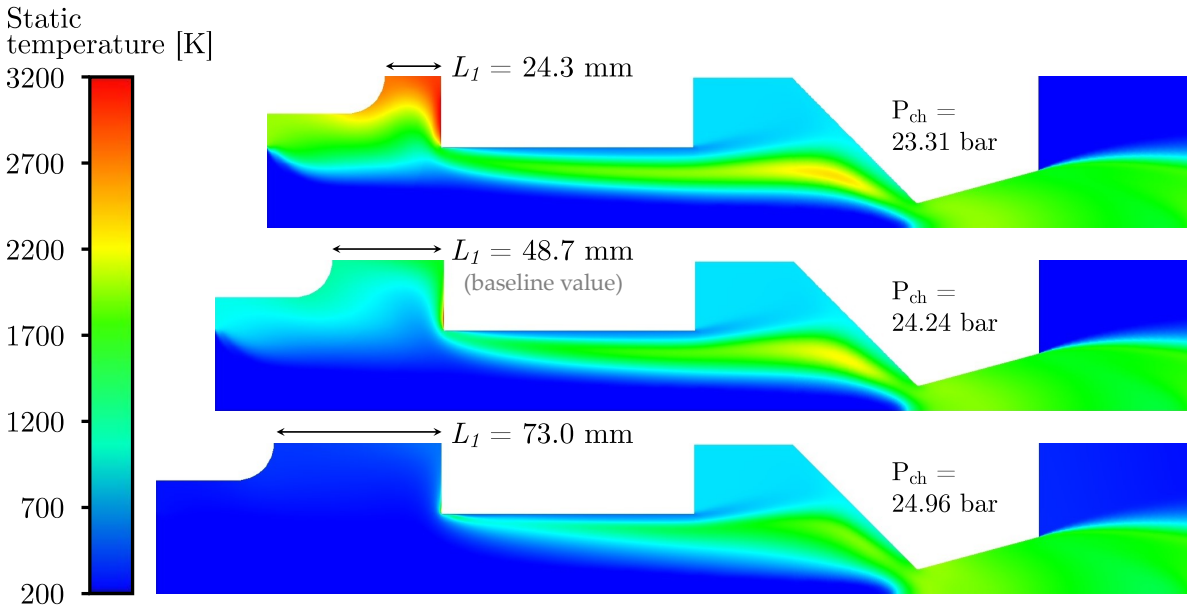

Fig. 3 Temperature fields for varying pre-combustion chamber lengths (L_1).

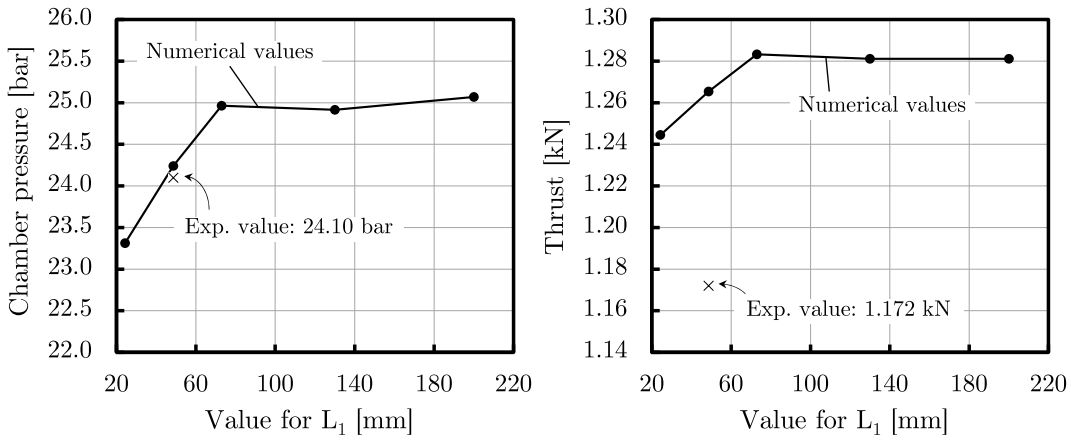

Fig. 4 Predicted influence of the pre-combustion chamber length L_1 on the operating conditions of the ULB-HRM: chamber pressure P_{ch} (left) and thrust F (right).

B. Post-combustion chamber

The influence of the post-combustion chamber length L_2, as indicated in Fig. 2, is now investigated. As in Section III.A, this is also done by increasing and decreasing its length by 50%. To provide additional insight, higher values for L_2 have been selected as well. Table 2 provides an overview of the selected post-combustion chamber lengths.

Table 2 Selected values for L_2 for the study of its influence on the operating conditions.

L_2 [mm]	Remark
21.5	baseline value −50%
43.0	baseline value
64.5	baseline value +50%
86.0	baseline value ×2
200.0	
430.0	baseline value ×10

Some of the resulting temperature fields are shown in Fig. 5. It is clear that the extension of the post-combustion chamber improves the development of the macroscopic diffusion flame, as it would be expected. The combustion reaction progress increases as the residence time of the reacting species increases with increasing L_2.

The effect of L_2 on the chamber pressure and thrust is shown in Fig. 6. Within the range of −50% to +50% offset of L_2 with respect to its baseline value of 43 mm, $P_{\text{ch,num}}$ and F_{num} vary quasi linearly with L_2. On Fig. 6, these are the three leftmost data points on both graphs. Within this range, a linear approximation results in the following relations for case SH4-04 of the ULB-HRM.

$$\frac{dP_{\text{ch,num}}}{dL_2} = 0.38 \text{ bar/cm} = (1.6\% \cdot P_{\text{ch,num (baseline)}}) \text{ bar/cm} \quad \text{for } L_2 \in [2.15, 6.45] \text{ cm} \tag{3}$$

$$\frac{dF_{\text{num}}}{dL_2} = 8.9 \text{ N/cm} = (0.8\% \cdot F_{\text{num (baseline)}}) \text{ N/cm} \quad \text{for } L_2 \in [2.15, 6.45] \text{ cm} \tag{4}$$

By comparing equations 1 and 2 with equations 3 and 4, it is concluded that L_2 has a slightly higher impact on the motor's operating conditions than L_1. This is true within the limits of the −50% and +50% deviations from their baseline values, for which equations 1–4 are valid. However, when comparing Fig. 4 with Fig. 6, it can be observed that, for values above +50%, the impact of L_2 becomes quite more important compared to that of L_1. Further extending the pre-combustion chamber (L_1) leads to a stagnation of $P_{\text{ch,num}}$ around 25 bar, whereas for the extension of the post-combustion chamber (L_2), the pressure keeps increasing up to 27.5 bar for a theoretical length of 43 cm. From this it is concluded that, in order to improve the performance of the ULB-HRM, the extension of the post-combustion chamber is preferable over the extension of the pre-combustion chamber.

C. Nozzle

In this section, a series of conical nozzles is under investigation by changing the parameters L_3, L_4, and α, as shown in Fig. 2. Only two of these parameters are independent, so, if one of them is kept constant, then the other two depend on each other. This is shown in Fig. 7, and for each of the three presented cases, a parametric study is done to observe the impact on the predicted thrust F_{num}. The baseline values for L_3 and L_4 are shown in Fig. 1, and they correspond to a nozzle half angle α of 15°. These baseline values represent the actual experimental nozzle that was used for case SH4-04, which is the reference case throughout this report. Based on ideal rocket propulsion theory [12], the predicted thrust F_{num} should be influenced by L_3, L_4, and α as the result of two main effects.

1) The resulting nozzle expansion area ratio $\epsilon = A_2/A_t$

   For an ideal rocket propulsion unit, an optimum value of ϵ exists such that the static pressure at the nozzle exit, P_2, is equal to the ambient pressure P_3. This leads to a maximum value for the thrust F. It could therefore be expected that the predicted thrust F_{num} increases whenever L_3, L_4, and α change in such a way that P_2 approaches P_3 (ϵ approaches its theoretical optimum). Some deviations are however possible, as the exhaust gasses in the model do not flow parallel with the nozzle axis, and as the flow chemistry in the nozzle is shifting instead of frozen.

2) The resulting direction of the velocity vectors at the nozzle exit

For an ideal rocket propulsion unit, it is assumed that all exhaust gasses leave the nozzle with a velocity parallel to the nozzle axis. If this is not the case, then only the x-components of the velocity vectors contribute to the thrust F. It is therefore expected that the predicted thrust F_{num} increases whenever L_3, L_4, and α change in such a way that the exhaust gasses velocity vectors approach the axial direction.

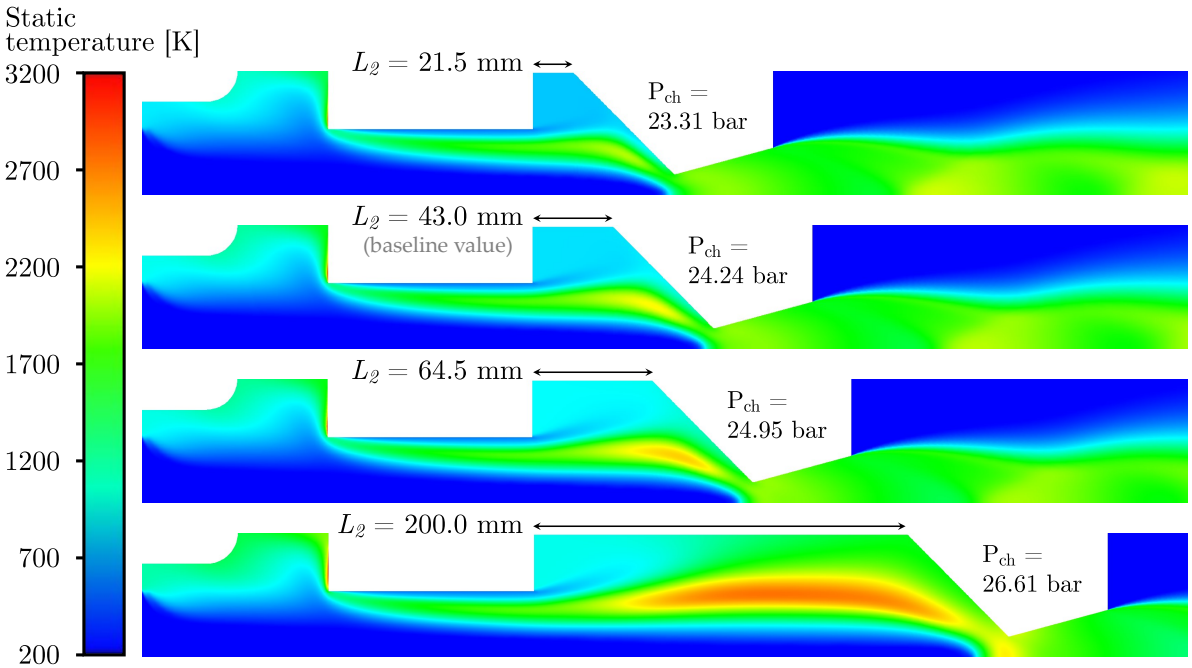

Fig. 5 Temperature fields for varying post-combustion chamber lengths (L_2).

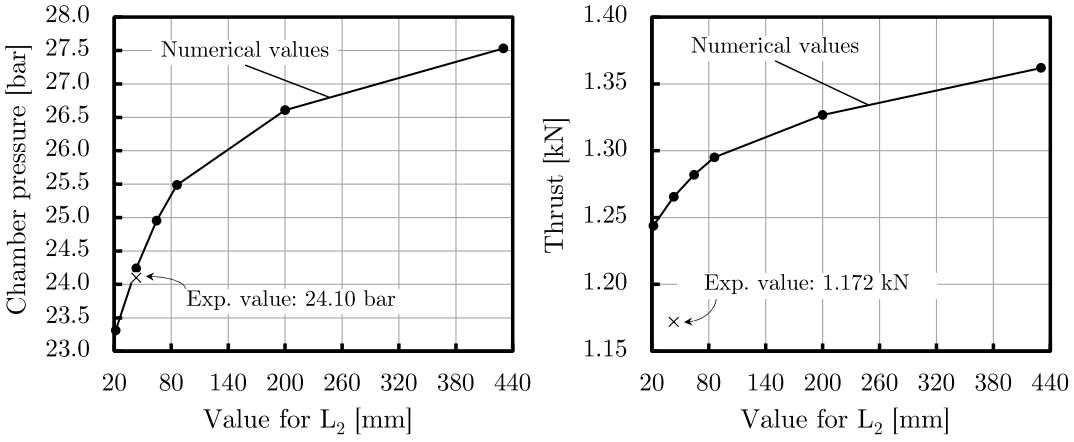

Fig. 6 Predicted influence of the post-combustion chamber length L_2 on the operating conditions of the ULB-HRM: chamber pressure P_{ch} (left) and thrust F (right).

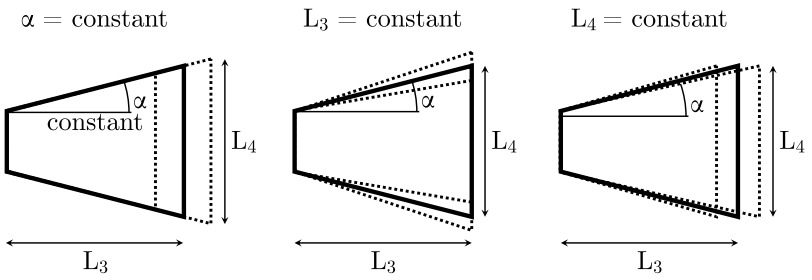

Fig. 7 Overview of the three parametric studies for the nozzle.

Figure 8 shows how the predicted thrust F_{num} is influenced by the studied nozzle dimensions. Note that the nozzle throat diameter, with a baseline value of 22 mm, is not under investigation. As a consequence, the chamber pressure $P_{\text{ch,num}}$ remains quasi constant for all simulations in this section, and is therefore not presented in the graphs.

When α is kept at its baseline value of 15° (solid curve on left diagram), a maximum thrust is observed for a nozzle exit diameter L_4 of 50 mm, which is the baseline value corresponding to the actual nozzle. The corresponding area-weighted static pressure at the nozzle exit P_2 = 107768 Pa, which is closer to the ambient pressure P_3 = 101325 Pa than any of the other data points on the curve. This corresponds to the expected behaviour of an ideal rocket propulsion unit.

Next, it is investigated how F_{num} responds to the nozzle exit diameter L_4 when the nozzle length L_3 is fixed (dashed curve on the left diagram in Fig. 8). An interesting observation is that F_{num} reaches a maximum for $\alpha = 11°$ and L_4 = 42.3 mm. These dimensions deviate from those of the actual nozzle, but the predicted gain in thrust is only 1%. The corresponding exit pressure P_2 is 168338 Pa, which is higher than P_3. In this case, the behaviour therefore deviates from that of an ideal rocket.

The right diagram on Fig. 8 shows how F_{num} changes with changing nozzle length L_3, while keeping the nozzle exit diameter L_4 constant at its baseline value of 50 mm. For these simulations, A_2/A_{t} is constant. Therefore, as expected, the nozzle exit pressure P_2 varies only very little, from 104193 Pa ($\alpha = 10°$) to 110494 Pa ($\alpha = 20°$). The corresponding nozzle lengths L_3 are 79 and 38 mm, respectively. The resulting curve shows that F_{num} varies quasi linearly with the nozzle half angle α within the investigated range. This behaviour is logical, as extending the nozzle with constant exit area simply implies that the gasses can undergo the same expansion but with a higher average value for v_x (x-component of velocity v), knowing that $v_x = v \cdot \cos\phi$ for a nozzle fluid element with velocity direction $\phi \in [0, \alpha]$. In this case, extending the existing nozzle from 52.25 to 79 mm while maintaining A_2/A_{t} results in a predicted increase in thrust of 2.5%.

From the above it can be concluded that the actual nozzle exit diameter of 50 mm seems adequate although the numerical model predicts a small increase in thrust (1%) if this value were to be reduced to 42 mm. This does however not seem opportune. Furthermore, the model confirms that a simple conical nozzle has the disadvantage of exhaust gasses not exiting the nozzle parallel to the nozzle axis. To increase the thrust and specific impulse, the existing nozzle could be extended, or a new bell-shaped nozzle could be fabricated.

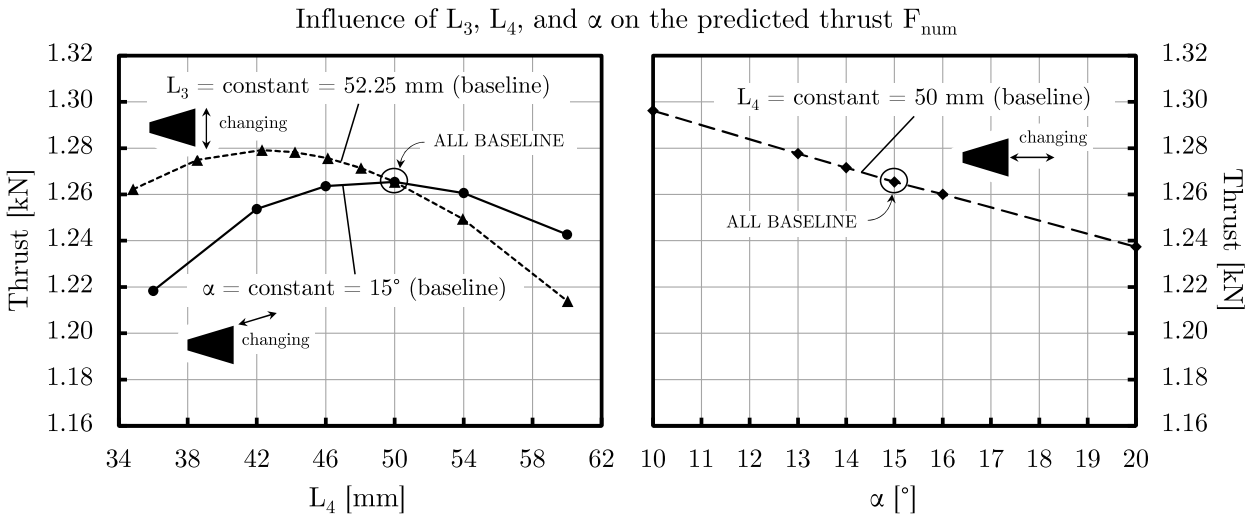

Fig. 8 Influence of the investigated nozzle dimensions on the predicted thrust F_{num}. On the left diagram, the impact of the nozzle exit diameter (L_4) is shown for two cases: constant α (nozzle half angle) and constant L_3 (nozzle length). On the right diagram, the impact of α is shown for a fixed nozzle exit diameter (L_4).

IV. Conclusions

A numerical parametric study of some of the geometrical dimensions of the 1 kN paraffin-fueled Hybrid Rocket Motor at Université Libre de Bruxelles (ULB-HRM) is presented. The numerical model, developed at the Royal Military Academy (RMA), is a two-phase model which takes entrained fuel droplets and oxidizer spray droplets into account.

The pre-combustion chamber length clearly has an impact on the extend to which a small part of the fuel is being recirculated in the pre-combustion chamber, where it reacts in an oxidizer rich region. Although the impact on the flowfield is therefore quite visible, the impact on the chamber pressure is limited to a maximum increase of about 1 bar when the pre-combustion chamber is extended by 50%. Any further extension does not contribute to the motor's performance in any way (the chamber pressure stagnates).

For the post-combustion chamber, an increase in length of 50% has a similar impact, as the chamber pressure also increases by about 1 bar. In this case, any further extension does lead to a further increase of the chamber pressure, but the rate of change of this pressure decreases with increasing length of the post-combustion chamber. This is a logical outcome, as its extension increases the residence time of the reacting species, which is beneficial for the reaction progress and the development of the macroscopic diffusion flame. For practical applications, however, very long post-combustion chambers are not opportune due to the increasing weight of the motor.

Next, the dimensions of the conical nozzle are under investigation. It is concluded that the existing nozzle expansion area ratio is adequate. Nevertheless, the CFD model predicts an increase in thrust when the nozzle length is increased. This is a logical behaviour, as an extension of the nozzle, without altering the expansion area ratio, increases the axial velocity of the exhaust gasses. Future work includes the design of a minimum length nozzle via the method of characteristics applied to a 2D axisymmetric flow. When this type of nozzle is designed properly, the exhaust gasses exit the nozzle parallel to the nozzle axis.

References

[1] Bouziane, M., Bertoldi, A. E. M., Milova, P., Hendrick, P., and Lefebvre, M., "Development and Testing of a Lab-scale Test-bench for Hybrid Rocket Motors," 2018 SpaceOps Conference, Marseille, France, May, 2018.

[2] Bouziane, M., Bertoldi, A. E. M., Dahae, L., Milova, P., Hendrick, P., and Lefebvre, M., "Design and Experimental Evaluation of Liquid Oxidizer Injection System for Hybrid Rocket Motors," 7th European Conference for Aeronautics and Space Sciences (EUCASS), Milan, Italy, May, 2017.

[3] Bouziane, M., Bertoldi, A. E. M., Dahae, L., Milova, P., Hendrick, P., and Lefebvre, M., "Experimental Investigation of Injectors Design and Their Effects on 1kN Performance Hybrid Rocket Motor," 69th International Astronautical Congress (IAC), Bremen, Germany, October, 2018.

[4] Bouziane, M., Bertoldi, A. E. D., Milova, P., Hendrick, P., and Lefebrve, M. H., "Performance Comparison of Oxidizer Injectors in a 1-kN Paraffin-Fueled Hybrid Rocket Motor," *Aerospace Science and Technology*, Vol. 89, 2019, pp. 392–406.

[5] Dequick, B., Lefebvre, M., and Hendrick, P., "CFD Simulation of a 1kN Paraffin-Fueled Hybrid Rocket Engine," AIAA Propulsion and Energy 2020 Forum (virtual event), August, 2020.

[6] Dequick, B., Lefebvre, M., and Hendrick, P., "Two-Phase CFD Simulation of a 1kN Paraffin-Fueled Hybrid Rocket Motor," AIAA Propulsion and Energy 2021 Forum (virtual event), August, 2021.

[7] Dequick, B., Lefebvre, M., and Hendrick, P., "Sensitivity Analysis of a Two-Phase CFD Simulation of a 1kN Paraffin-Fueled Hybrid Rocket Motor," *Energies*, Vol. 14, 2021, p. 6794.

[8] Jones, W. P., and Launder, B. E., "The Prediction of Laminarization with a Two-Equation Model of Turbulence," *Int. Journal for Heat and Mass Transfer*, Vol. 15, 1972.

[9] Magnussen, B. F., and Hjertager, B. H., "On Mathematical Modeling of Turbulent Combustion With Special Emphasis on Soot Formation and Combustion," 1977.

[10] Volk, F., and Bathelt, H., *User's Manual for the ICT-Thermodynamic Code*, Fraunhofer Institute for Chemical Technology, 1991.

[11] Gordon, S., and McBride, B. J., *Computer Program for Calculation of Complex Chemical Equilibrium Compositions and Applications*, NASA Reference Publication 1311, 1996.

[12] Sutton, G. P., and Biblarz, O., *Rocket Propulsion Elements*, 9th ed., 2017, pp. 45–98.